

MOX–Report No. 06/2010

**The effect of visco-elasticity and other physical properties on aortic and cerebral pulse waveforms: an analytical and numerical study**

JORDI ALASTRUEY, TIZIANO PASSERINI,  
LUCA FORMAGGIA, JOAQUIM PEIRÓ

MOX, Dipartimento di Matematica “F. Brioschi”  
Politecnico di Milano, Via Bonardi 9 - 20133 Milano (Italy)

[mox@mate.polimi.it](mailto:mox@mate.polimi.it)

<http://mox.polimi.it>



# The effect of visco-elasticity and other physical properties on aortic and cerebral pulse waveforms: an analytical and numerical study

Jordi Alastruey<sup>\*1,2</sup>, Tiziano Passerini<sup>3,4</sup>, Luca Formaggia<sup>3</sup>, Joaquim Peiró<sup>2</sup>

<sup>1</sup>Department of Bioengineering,  
Imperial College London, SW7 2AZ, UK

<sup>2</sup>Department of Aeronautics,  
Imperial College London, SW7 2AZ, UK

<sup>3</sup>MOX, Dipartimento di Matematica F. Brioschi,  
Politecnico di Milano, Italy

<sup>4</sup>Department of Mathematics and Computer Science,  
Emory University, USA

January 2010

## Abstract

The nonlinear one-dimensional equations of blood flow in Voigt-type visco-elastic vessels are numerically solved using both a Taylor-Galerkin and a discontinuous Galerkin scheme to study the effects on aortic and cerebral pulse waveforms of wall visco-elasticity, fluid viscosity, wall compliances and resistances, flow inertia, cardiac ejection, and outflow pressure. A linear analysis of these equations shows that wave dispersion and dissipation is caused by wall viscosity at high frequencies and fluid viscosity at low frequencies. During approximately the last three fourths of diastole the inertial effects of the flow can be neglected, and pressures tend to a space-independent shape dictated by global quantities (cardiac ejection, total peripheral resistance and compliance, and outflow pressure) and the viscous modulus of each arterial segment. During this period, the area-pressure curve reduces to a line whose slope provides a better approximation to the local pulse wave speed than do current techniques based on simultaneous pressure and velocity measurements. The viscous modulus can be estimated from the area of the area-pressure loop. Our findings are important for the identification and estimation of haemodynamic quantities related to the prevention, diagnosis and treatment of disease.

*Keywords:* Pulse wave propagation; pulse wave speed; circulatory system; circle of Willis; one-dimensional modelling; Voigt-type visco-elasticity; Taylor-Galerkin methods; discontinuous Galerkin methods.

---

\*Corresponding author. E-mail addresses: [jordi.alastruey-arimon@imperial.ac.uk](mailto:jordi.alastruey-arimon@imperial.ac.uk) (J. Alastruey), [tiziano.passerini@gmail.com](mailto:tiziano.passerini@gmail.com) (T. Passerini), [luca.formaggia@polimi.it](mailto:luca.formaggia@polimi.it) (L. Formaggia), [j.peiro@imperial.ac.uk](mailto:j.peiro@imperial.ac.uk) (J. Peiró).

# 1 Introduction

One-dimensional (1-D) reduced modelling of flow in the arterial system is commonly applied to simulate, at reasonable computational cost, the evolution of area-averaged values of blood pressure and flow along the axial direction of larger arteries produced by the contraction of the heart [30, 31]. These changes propagate in the form of pulse waves, which carry valuable information on the functionality and morphology of the cardiovascular system. Through 1-D modelling we can study haemodynamic problems that cannot be addressed *in vivo* for technical and physiological reasons; e.g. some vessels are inaccessible, manipulation of the properties of interest can be dangerous or can elicit reflex compensation, and several parameters of interest are not directly measurable. It has been shown that the 1-D formulation can provide valuable insight into the development of methods for the diagnosis of disease [3, 8, 20, 37] and the identification of anatomical variations [4, 5] by wave analysis, and into improving the accuracy of the boundary conditions used in three-dimensional simulations of localised areas of the vasculature [17, 27–29].

Arterial walls are anisotropic and heterogeneous, composed of layers with different biomechanical characteristics whose stress-strain relationships are nonlinear and exhibit creep, stress relaxation and hysteresis [21, Chap. 8]. However, an instantaneous static equilibrium based on Laplace’s law is commonly assumed in 1-D modelling to describe the dynamics of the arterial wall. This approach is able to capture most of the features of pulse waveforms in normal physiological conditions [25, 26, 36], because the pulse wave speed calculated with a purely elastic wall model closely matches the wave speed measured *in vivo* [23].

More sophisticated representations of the arterial wall have been proposed in reduced modelling to improve the agreement between *in vivo* and numerical pulse waveforms, such as a Voigt-type visco-elastic model that features hysteresis and creep [9, 10, 14, 40]. Models accounting also for stress relaxation (which is not modelled by the Voigt model) have been proposed [11, 16, 38], but the applicability of these models to patient-specific 1-D modelling is limited because of the difficulty in estimating their multiple parameters from *in vivo* data.

The aim of this work is to incorporate a Voigt-type visco-elastic model of the arterial wall into the Taylor-Galerkin (TG) and the discontinuous Galerkin (DG) schemes previously developed and validated to solve the 1-D equations of blood flow in elastic vessels [18, 25, 33, 34], to study the effects of wall visco-elasticity, fluid viscosity, arterial compliances and resistances, blood inertia, cardiac ejection, and outflow pressure on pulse waveforms in large arteries in normal physiological conditions, and to describe a method to estimate the local compliance and viscous modulus of an artery from simultaneous pressure and diameter measurements. The choice of this type of visco-elastic model is particularly convenient because it requires the esti-

mation of only one viscous parameter in addition to the geometry and wall stiffness of the artery, and it is justified because of its ability to reproduce the main features of visco-elastic effects on blood flow.

We first introduce the nonlinear 1-D equations that govern blood flow in Voigt-type visco-elastic arterial networks and we detail their numerical solution using both a TG and a DG scheme. We then perform a linear analysis of these equations to study the effects on arterial pulse waveforms of different physical properties of the cardiovascular system. We will distinguish between the effects on blood flow in a single artery, referred to as *local effects*, and in the arterial network as a whole, referred to as *global effects*. We finally describe a method to estimate the local arterial compliance and viscous modulus from simultaneous pressure and diameter measurements. The results of our analysis will be illustrated in a single-vessel model of the human aorta and in a model of the larger human conduit arteries in the thorax and head, including the circle of Willis (a ring-like arterial structure located at the base of the brain, Figure 1).

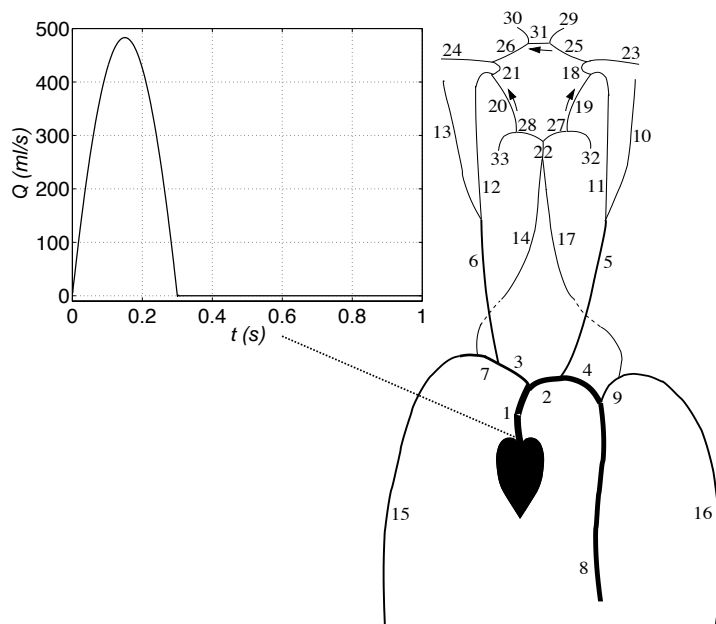


Figure 1: Schematic representation of the 33-arteries network used to simulate pulse wave propagation in the cerebral circulation. Their names and properties are shown in Table 1. A periodic half-sinusoidal flow wave is prescribed at the inlet of the ascending aorta. (Modified from [4].)

Arterial segment	Length (cm)	Radius (mm)	$\tilde{c}_i$ (m s <sup>-1</sup> )	$R$ (GPa s m <sup>-3</sup> )	$Z_0$ (GPa s m <sup>-3</sup> )	$C$ (10 <sup>-10</sup> m <sup>3</sup> Pa <sup>-1</sup> )
1. Asc aorta	4.0	12.0	5.9	-	-	-
2. Aortic arch I	2.0	11.2	5.3	-	-	-
3. Brachiocephalic	3.4	6.2	5.7	-	-	-
4. Aortic arch II	3.9	10.7	5.2	-	-	-
5. L. carotid	20.8	2.5	8.0	-	-	-
6. R. carotid	17.7	2.5	8.0	-	-	-
7. R. subclavian	3.4	4.2	6.3	-	-	-
8. Thoracic aorta	15.6	10.0	5.3	0.18	0.02	38.7
9. L. subclavian	3.4	4.2	6.3	-	-	-
10. L. ext. carotid	17.7	1.5	11.3	5.43	1.67	1.27
11. L. int. carotid I	17.7	2.0	11.3	-	-	-
12. R. int. carotid I	17.7	2.0	11.3	-	-	-
13. R. ext. carotid	17.7	1.5	11.3	5.43	1.67	1.27
14. R. vertebral	14.8	1.35	11.3	-	-	-
15. R. brachial	42.2	4.03	6.5	2.68	0.13	2.58
16. L. brachial	42.2	4.0	6.5	2.68	0.13	2.58
17. L. vertebral	14.8	1.35	11.3	-	-	-
18. L. int. carotid II	0.5	2.0	15.9	-	-	-
19. L. PCoA	1.5	0.7	15.9	-	-	-
20. R. PCoA	1.5	0.7	15.9	-	-	-
21. R. int. carotid II	0.5	2.0	15.9	-	-	-
22. Basilar	2.9	1.6	11.3	-	-	-
23. L. MCA	11.9	1.4	15.9	5.97	2.605	1.16
24. R. MCA	11.9	1.4	15.9	5.97	2.605	1.16
25. L. ACA, A1	1.2	1.2	15.9	-	-	-
26. R. ACA, A1	1.2	1.2	15.9	-	-	-
27. L. PCA, A1	0.5	1.1	15.9	-	-	-
28. R. PCA, A1	0.5	1.1	15.9	-	-	-
29. L. ACA, A2	10.3	1.2	15.9	8.48	3.70	0.815
30. R. ACA, A2	10.3	1.2	15.9	8.48	3.70	0.815
31. ACoA	0.3	0.7	15.9	-	-	-
32. L. PCA, P2	8.6	1.05	15.9	11.08	4.83	0.62
33. R. PCA, P2	8.6	1.05	15.9	11.08	4.83	0.62

Table 1: Lengths, initial radii, inviscid wave speeds  $\tilde{c}_i$ , and peripheral resistances  $R$ , characteristic impedances  $Z_0 = \rho\tilde{c}_i/A_0$  and compliances  $C$  of the 33 arteries of the cerebral circulation depicted in Figure 1. In all the arterial segments,  $\rho = 1050$  Kg m<sup>-3</sup>,  $\mu = 4.5$  mPa s and  $\tilde{\gamma} = 0.3$  MPa s m<sup>-1</sup>, based on the data provided in [4, 10].

## 2 Methodology

The nonlinear governing equations of the 1-D incompressible flow in a compliant vessel are [31]

$$\begin{cases} \frac{\partial A}{\partial t} + \frac{\partial Q}{\partial x} = 0 \\ \frac{\partial Q}{\partial t} + \frac{\partial}{\partial x} \left( \alpha \frac{Q^2}{A} \right) + \frac{A}{\rho} \frac{\partial P}{\partial x} = \frac{f}{\rho} \end{cases}, \quad (1)$$

where  $x$  is the axial coordinate along the vessel,  $t$  denotes the time,  $A(x, t)$  is the cross-sectional area of the lumen,  $Q(x, t)$  the mass flux across it,  $P(x, t)$  represents the average internal pressure over the cross section,  $\alpha$  is the momentum-flux correction coefficient (hereafter we will take  $\alpha = 1$ )<sup>1</sup>, and  $\rho$  is the constant mass density of blood. The friction force per unit length  $f(x, t)$  is given by [35, 39]

$$f = 2\mu\pi\widehat{R} \left[ \frac{\partial u}{\partial r} \right]_{r=\widehat{R}}, \quad (2)$$

where  $\mu$  is the constant blood viscosity,  $\widehat{R}(x, t)$  is the lumen radius, and  $u(x, r, t)$  is the axial axisymmetric velocity ( $r$  is the radial coordinate). A typical profile for axisymmetric flow satisfying the no-slip condition is

$$u = U \frac{\zeta + 2}{\zeta} \left[ 1 - \left( \frac{r}{\widehat{R}} \right)^\zeta \right], \quad (3)$$

where  $U(x, t) = Q/A$  is the average axial velocity and  $\zeta$  is a constant. Substitution of Equation (3) into (2) yields  $f = -2(\zeta + 2)\mu\pi U$ . Following [35],  $\zeta = 9$  provides a good compromise fit to experimental findings. Notice that  $\zeta = 2$  corresponds to a parabolic profile which leads to Poiseuille's flow resistance  $f = -8\mu\pi U$ .

System (1) is typically closed by defining an explicit algebraic relationship between  $P$  and  $A$ . Here we use a relation of the form

$$P = \mathcal{F}(A; x, t),$$

where the function  $\mathcal{F}$  depends on the model used to simulate the dynamics of the arterial wall.

---

<sup>1</sup>This is a common assumption that leads to considerable mathematical simplifications. It is equivalent to assuming a flat velocity profile, which is a reasonable assumption according to experimental data [35].

The system of equations (1) can be alternatively expressed in terms of the variables  $(A, U)$ . By simple manipulation one gets

$$\begin{cases} \frac{\partial A}{\partial t} + \frac{\partial(AU)}{\partial x} = 0 \\ \frac{\partial U}{\partial t} + U \frac{\partial U}{\partial x} + \frac{1}{\rho} \frac{\partial P}{\partial x} = \frac{f}{\rho A} \end{cases}. \quad (4)$$

## 2.1 Visco-elastic model of the arterial wall

The dynamics of the arterial wall can be modelled using a linearised generalized string model of the form [18, 32]

$$P = P_{ext} + \frac{\beta}{A_0}(\sqrt{A} - \sqrt{A_0}) + \gamma \frac{\partial A}{\partial t} + m \frac{\partial^2 A}{\partial t^2} - a \frac{\partial^2}{\partial x^2}(\sqrt{A} - \sqrt{A_0}), \quad (5)$$

$$\beta(x) = \frac{4}{3}\sqrt{\pi}hE, \quad \gamma(x) = \frac{\tilde{\gamma}}{2\sqrt{\pi}A_0}, \quad m(x) = \frac{\rho_w h}{2\sqrt{\pi}A_0}, \quad a(x) = \frac{\tilde{a}}{\sqrt{\pi}},$$

where  $P_{ext}$  denotes the external pressure. This model assumes a thin, homogeneous, incompressible and visco-elastic arterial wall deforming axisymmetrically, in which each cross-section is independent of the others, with a thickness  $h(x)$ , a Young's modulus  $E(x)$ , a lumen area  $A_0(x)$  at the reference state  $(P, U) = (P_{ext}, 0)$ , a Voigt-type viscous modulus  $\tilde{\gamma}(x)$ , and a wall mass density  $\rho_w(x)$ . The coefficient  $\tilde{a}(x)$  is related to the longitudinal pre-stress state of the vessel. In this work we will consider  $P_{ext} = 0$ ,  $m = 0$  and  $a = 0$ , which leads to the visco-elastic tube law

$$P = \frac{\beta}{A_0}(\sqrt{A} - \sqrt{A_0}) + \gamma \frac{\partial A}{\partial t}. \quad (6)$$

Despite its limitations, Equation (6) is able to reproduce the main features of pulse waveforms observed *in vivo* in large arteries [9, 10, 14, 40].

## 2.2 Numerical solutions

Although the viscous term in Equation (6) breaks the hyperbolic nature of Systems (1) and (4), they can be solved using a TG or a DG scheme because the elastic term in Equation (6) is dominant under normal physiological conditions. If we assume  $\gamma$  to be constant in Equation (6) and we consider  $\frac{\partial A}{\partial t} = -\frac{\partial Q}{\partial x}$ , which follows from conservation of mass, System (1) can be written in the non-conservative form

$$\frac{\partial \mathbf{Q}}{\partial t} + \mathbf{H}_e \frac{\partial \mathbf{Q}}{\partial x} + \mathbf{H}_v \frac{\partial^2 \mathbf{Q}}{\partial x^2} = \mathbf{S}_Q, \quad (7)$$

with

$$\mathbf{Q} = \begin{bmatrix} A \\ Q \end{bmatrix}, \quad \mathbf{S}_Q = \begin{bmatrix} 0 \\ \frac{f}{\rho} + \frac{A}{\rho A_0} \left( A_0^{\frac{1}{2}} - A^{\frac{1}{2}} \right) \frac{d\beta}{dx} + \frac{\beta A}{\rho A_0^2} \left( A^{\frac{1}{2}} - \frac{1}{2} A_0^{\frac{1}{2}} \right) \frac{dA_0}{dx} \end{bmatrix},$$

$$\mathbf{H}_e = \begin{bmatrix} 0 & 1 \\ \tilde{c}_i^2 - \left( \frac{Q}{A} \right)^2 & 2 \frac{Q}{A} \end{bmatrix}, \quad \mathbf{H}_v = \begin{bmatrix} 0 & 0 \\ 0 & -\frac{\gamma A}{\rho} \end{bmatrix},$$

and  $\tilde{c}_i = \sqrt{\frac{\beta}{2\rho A_0}} A^{1/4}$  is the speed of pulse wave propagation when the wall is purely elastic and the fluid inviscid [33]. In what follows, we will refer to it as the inviscid pulse wave speed.

System (4) can be written in the following conservative form

$$\frac{\partial \mathbf{U}}{\partial t} + \frac{\partial \mathbf{F}}{\partial x} = \mathbf{S}_U, \quad (8)$$

with

$$\mathbf{U} = \begin{bmatrix} A \\ U \end{bmatrix}, \quad \mathbf{S}_U = \begin{bmatrix} 0 \\ \frac{f}{\rho A} \end{bmatrix},$$

$$\mathbf{F} = \mathbf{F}_e + \mathbf{F}_v = \begin{bmatrix} UA \\ \frac{U^2}{2} + \frac{P_e}{\rho} \end{bmatrix} + \begin{bmatrix} 0 \\ -\frac{\gamma}{\rho} \frac{\partial(AU)}{\partial x} \end{bmatrix},$$

and  $P_e = \frac{\beta}{A_0} (\sqrt{A} - \sqrt{A_0})$  being the elastic component of pressure. The flux  $\mathbf{F}$  has been separated into an elastic ( $\mathbf{F}_e$ ) and a viscous ( $\mathbf{F}_v$ ) term. Similarly we distinguish between elastic ( $\mathbf{H}_e$ ) and viscous ( $\mathbf{H}_v$ ) terms in Equation (7).

Section 2.2.1 shows how to solve Equation (7) using a TG scheme, and Section 2.2.2 shows how to solve Equation (8) using a DG scheme. Unless it is specified otherwise, the treatment of boundary conditions and bifurcations in both schemes is the same as described in [18,28,31] for the TG and [2,6,31,34] for the DG using the elastic tube law (i.e.  $\gamma = 0$  in Equation (6)).

### 2.2.1 Taylor-Galerkin scheme

We use an operator-splitting approach by which Equation (7) becomes

$$\begin{cases} \frac{\partial \hat{\mathbf{Q}}}{\partial t} + \mathbf{H}_e \frac{\partial \mathbf{Q}}{\partial x} = \mathbf{S}_Q \\ \frac{\partial \tilde{Q}}{\partial t} - \frac{\gamma A}{\rho} \frac{\partial^2 Q}{\partial x^2} = 0 \end{cases}, \quad (9)$$

with  $\hat{\mathbf{Q}} = [A \quad \hat{Q}]^T$  and  $Q = \hat{Q} + \tilde{Q}$  [18]. We now consider the following conservation form for the hyperbolic system in (9)

$$\frac{\partial \hat{\mathbf{Q}}}{\partial t} + \frac{\partial \mathbf{G}_e}{\partial x} = \mathbf{B}, \quad (10)$$

with

$$\mathbf{G}_e = \begin{bmatrix} Q \\ \frac{Q^2}{A} + \frac{\beta}{3\rho A_0} A^{\frac{3}{2}} \end{bmatrix},$$

$$\mathbf{B} = \begin{bmatrix} 0 \\ \frac{f}{\rho} + \frac{A}{\rho A_0} \left( A_0^{\frac{1}{2}} - \frac{2}{3} A^{\frac{1}{2}} \right) \frac{d\beta}{dx} + \frac{\beta A}{\rho A_0^2} \left( \frac{2}{3} A^{\frac{1}{2}} - \frac{1}{2} A_0^{\frac{1}{2}} \right) \frac{dA_0}{dx} \end{bmatrix}.$$

We discretise Equation (10) by a second-order TG scheme. This choice is motivated by the excellent dispersion error characteristic of the scheme and its simplicity of implementation [18]. For each time interval  $[t^n, t^{n+1}]$  ( $n = 0, 1, \dots$ ), we obtain the following approximation  $\widehat{\mathbf{Q}}^{n+1}$  of  $\widehat{\mathbf{Q}}$  at time  $t^{n+1}$

$$\begin{aligned} \widehat{\mathbf{Q}}^{n+1} &= \widehat{\mathbf{Q}}^n - \Delta t \frac{\partial}{\partial x} \left[ \mathbf{G}_e^n + \frac{\Delta t}{2} \mathbf{G}_e^n \widehat{\mathbf{Q}} \mathbf{B}^n \right] \\ &\quad - \frac{\Delta t^2}{2} \left[ \mathbf{B}_{\widehat{\mathbf{Q}}}^n \frac{\partial \mathbf{G}_e^n}{\partial x} - \frac{\partial}{\partial x} \left( \mathbf{G}_e^n \widehat{\mathbf{Q}} \frac{\partial \mathbf{G}_e^n}{\partial x} \right) \right] + \Delta t \left( \mathbf{B}^n + \frac{\Delta t}{2} \mathbf{B}_{\widehat{\mathbf{Q}}}^n \mathbf{B}^n \right), \end{aligned} \quad (11)$$

where the superscript  $n$  indicates quantities computed at time  $t^n$ ,  $\Delta t = t^{n+1} - t^n$  and

$$\mathbf{G}_e^n \widehat{\mathbf{Q}} = \frac{\partial \mathbf{G}_e}{\partial \mathbf{Q}}(\widehat{\mathbf{Q}}^n), \quad \mathbf{B}_{\widehat{\mathbf{Q}}}^n = \frac{\partial \mathbf{B}}{\partial \mathbf{Q}}(\widehat{\mathbf{Q}}^n).$$

To compute  $\widehat{\mathbf{Q}}^{n+1}$  we take  $\widehat{\mathbf{Q}}^n = \mathbf{Q}^n$  and  $\widetilde{\mathbf{Q}}^n = 0$  (i.e. the mass flux correction  $\widetilde{\mathbf{Q}}$  is not propagated from the previous time interval).

Application of the Galerkin finite element method to Equation (11) in a domain  $\Omega = [a, b]$  discretised into a mesh of  $N_{el}$  elemental non-overlapping regions  $\Omega_e = [x_e^l, x_e^u]$ , such that  $h = x_e^u - x_e^l$  is the (uniform) grid size,  $x_e^u = x_{e+1}^l$  for  $e = 1, \dots, N_{el} - 1$ , and

$$\bigcup_{e=1}^{N_{el}} \Omega_e = \Omega,$$

yields

$$\begin{aligned} \left( \widehat{\mathbf{Q}}_h^{n+1}, \boldsymbol{\psi}_h \right)_\Omega &= \left( \widehat{\mathbf{Q}}_h^n, \boldsymbol{\psi}_h \right)_\Omega + \Delta t \left( \mathbf{G}_e^n_{LW}, \frac{\partial \boldsymbol{\psi}_h}{\partial x} \right)_\Omega - \frac{\Delta t^2}{2} \left( \mathbf{B}_{\widehat{\mathbf{Q}}}^n \frac{\partial \mathbf{G}_e^n}{\partial x}, \boldsymbol{\psi}_h \right)_\Omega \\ &\quad - \frac{\Delta t^2}{2} \left( \mathbf{G}_e^n \widehat{\mathbf{Q}} \frac{\partial \mathbf{G}_e^n}{\partial x}, \frac{\partial \boldsymbol{\psi}_h}{\partial x} \right)_\Omega + \Delta t \left( \mathbf{B}_{LW}^n, \boldsymbol{\psi}_h \right)_\Omega, \quad \forall \boldsymbol{\psi}_h \in \mathbf{V}_h^0, \end{aligned} \quad (12)$$

In Equation (12),  $\widehat{\mathbf{Q}}_h$  and  $\boldsymbol{\psi}_h$  denote the approximation of  $\widehat{\mathbf{Q}}$  and test functions  $\boldsymbol{\psi}$ , respectively, in the finite space  $\mathbf{V}_h^0$  of continuous piecewise polynomial vector functions (built on the given mesh), which are zero at the boundary,

$$(\mathbf{u}, \mathbf{v})_\Omega = \int_\Omega \mathbf{u} \cdot \mathbf{v} \, dx$$

is the standard  $\mathbf{L}^2(\Omega)$  inner product and

$$\begin{aligned}\mathbf{G}_{eLW} &= \mathbf{G}_e + \frac{\Delta t}{2} \mathbf{G}_{e\hat{\mathbf{Q}}}\mathbf{B}, \\ \mathbf{B}_{LW} &= \mathbf{B} + \frac{\Delta t}{2} \mathbf{B}_{\hat{\mathbf{Q}}}\mathbf{B}.\end{aligned}$$

The second equation in (9) is used to correct the mass flux. The finite element formulation for this equation reads as follows [18]: given  $A_h^{n+1}$  and  $\hat{Q}_h^{n+1}$ , find  $\tilde{Q}_h^{n+1} \in V_h^0$  such that

$$\begin{aligned}\left(\frac{1}{A_h^{n+1}}\tilde{Q}_h^{n+1}, \psi_h\right)_\Omega + \Delta t \frac{\gamma}{\rho} \left(\frac{\partial \tilde{Q}_h^{n+1}}{\partial x}, \frac{\partial \psi_h}{\partial x}\right)_\Omega = \\ - \Delta t \frac{\gamma}{\rho} \left(\frac{\partial \hat{Q}_h^{n+1}}{\partial x}, \frac{\partial \psi_h}{\partial x}\right)_\Omega, \quad \forall \psi_h \in V_h^0, \quad (13)\end{aligned}$$

which corresponds to having imposed a homogeneous Dirichlet boundary condition for the correction term  $\tilde{Q}$ . In other words, we assume that the mass flux correction is only active inside the computational domain.

## 2.2.2 Discontinuous Galerkin scheme

This is a convenient scheme for high-order discretisation of hyperbolic conservation laws for convection-dominated flows [13], such as arterial flows. It allows us to propagate waves of different frequencies without suffering from excessive dispersion and diffusion errors.

The DG discrete form of System (8) in the previously defined domain  $\Omega$  is given by [34]

$$\begin{aligned}\left(\frac{\partial \mathbf{U}^\delta}{\partial t}, \boldsymbol{\psi}^\delta\right)_{\Omega_e} + \left(\frac{\partial \mathbf{F}(\mathbf{U}^\delta)}{\partial x}, \boldsymbol{\psi}^\delta\right)_{\Omega_e} + \\ + \sum_{e=1}^{N_{el}} \left[\boldsymbol{\psi}^\delta \cdot \left\{\mathbf{F}^u - \mathbf{F}(\mathbf{U}^\delta)\right\}\right]_{x_e^l}^{x_e^u} = \left(\mathbf{S}_U^\delta, \boldsymbol{\psi}^\delta\right)_{\Omega_e}, \quad \forall \boldsymbol{\psi}^\delta \in \mathbf{V}^\delta,\end{aligned}$$

where  $\mathbf{U}^\delta$  and  $\boldsymbol{\psi}^\delta$  denote the approximation of  $\mathbf{U}$  and test functions  $\boldsymbol{\psi}$ , respectively, in the finite space  $\mathbf{V}^\delta$  of piecewise polynomial vector functions (they may be discontinuous across inter-element boundaries), and  $\mathbf{F}^u = \mathbf{F}_e^u + \mathbf{F}_v^u$  is the approximation of the flux at the interface.

The term  $\mathbf{F}_e^u$  is treated through the solution of a Riemann problem, as discussed in [2, 33]. The term  $\mathbf{F}_v^u$  requires a different treatment. Various ways of dealing with this term are analysed in [43]. Here we approximate  $\mathbf{F}_v^u$  at the inter-element boundaries as

$$\mathbf{F}_v^u|_{x_e^u} = \mathbf{F}_v^u|_{x_{e+1}^l} = \frac{1}{2} \left(\mathbf{F}_v|_{x_e^u} + \mathbf{F}_v|_{x_{e+1}^l}\right),$$

with  $\mathbf{F}_v^u|_{x_1^l} = \mathbf{F}_v|_{x_1^l}$  at the inlet of the domain and  $\mathbf{F}_v^u|_{x_{Nel}^u} = \mathbf{F}_v|_{x_{Nel}^u}$  at the outlet, so that  $\mathbf{F}_v^u - \mathbf{F}_v(\mathbf{U}^\delta) = 0$  at both boundaries.

The expansion bases are selected to be a polynomial space of order  $P$  and the solution is expanded on each region  $\Omega_e$  in terms of Legendre polynomials  $L_p(\xi)$ , i.e.

$$\mathbf{U}^\delta|_{\Omega_e}(x_e(\xi), t) = \sum_{p=0}^P L_p(\xi) \widehat{\mathbf{U}}_e^p,$$

where  $\widehat{\mathbf{U}}_e^p(t)$  are the expansion coefficients. Following standard finite element techniques, we consider  $\xi$  in the reference element  $\Omega_{st} = \{-1 \leq \xi \leq 1\}$  and introduce the elemental affine mapping

$$x_e(\xi) = x_e^l \frac{(1 - \xi)}{2} + x_e^u \frac{(1 + \xi)}{2}.$$

The choice of discontinuous discrete solution and test functions allow us to decouple the problem on each element, the only link coming through the boundary fluxes. Legendre polynomials are particularly convenient because the basis is orthogonal with respect to the  $L^2(\Omega_e)$  inner product. The discretisation in time is performed by a second-order Adams-Bashforth scheme.

### 2.3 Linear analysis

We will focus in the following on the effects of the parameters of the model on pulse waveforms. When considering a single artery, we will refer to *local* effects (Section 2.3.1), while *global* effects will apply to the arterial network as a whole (Section 2.3.2). To simplify the analysis, a linear formulation is obtained as follows. Equations (1) and (6) are linearised about the reference state  $(A, P, Q) = (A_0, 0, 0)$ , with  $\beta$ ,  $A_0$  and  $\gamma$  constant along  $x$ , which yields

$$\begin{cases} C_{1D} \frac{\partial p_e}{\partial t} + \frac{\partial q}{\partial x} = 0, \\ L_{1D} \frac{\partial q}{\partial t} + \frac{\partial p_e}{\partial x} - \gamma \frac{\partial^2 q}{\partial x^2} = -R_{1D} q, \\ p = p_e - \gamma \frac{\partial q}{\partial x}, \quad p_e = \frac{a}{C_{1D}}, \end{cases} \quad (14)$$

where  $a$ ,  $p$ ,  $p_e$  and  $q$  are the perturbation variables for area, pressure, elastic component of pressure and flow rate, respectively, i.e.  $(A, P, P_e, Q) = (A_0 + a, p, p_e, q)$ , and

$$R_{1D} = \frac{2(\zeta + 2)\pi\mu}{A_0^2}, \quad L_{1D} = \frac{\rho}{A_0}, \quad C_{1D} = \frac{2A_0^{3/2}}{\beta} \quad (15)$$

are the resistance to flow due to fluid viscosity, blood inertia and elastic wall compliance, respectively, per unit length of vessel.

### 2.3.1 Local effects

Following [28, Chap. 2] and [22, Chap. 6] we derive an analytical solution to the system of equations (14) under the assumption of periodicity, which allows us to write  $p_e$  and  $q$  as the harmonic waves<sup>2</sup>

$$p_e(x, t) = \widehat{p}_e e^{I(\omega t - kx)}, \quad q(x, t) = \widehat{q} e^{I(\omega t - kx)}, \quad (16)$$

where  $I = \sqrt{-1}$ ,  $k$  is the wave number,  $\omega$  is the angular frequency (assumed to be real), and  $\widehat{p}_e$  and  $\widehat{q}$  are the pressure and flow wave amplitudes at  $(x, t) = (0, 0)$ , respectively. Substitution of Equations (16) into the first two equations of System (14) and combination of the resulting expressions yields

$$L_{1D}\omega^2 - (\gamma k^2 + R_{1D})I\omega - \frac{k^2}{C_{1D}} = 0, \quad (17)$$

which provides the following relation between  $\omega$  and  $k$

$$\omega = \frac{I(\gamma k^2 + R_{1D}) \pm \sqrt{-(\gamma k^2 + R_{1D})^2 + 4k^2 \frac{L_{1D}}{C_{1D}}}}{2L_{1D}}.$$

The resulting phase velocity  $c_p = \omega/k$  is

$$c_p = \frac{I\left(\gamma k + \frac{R_{1D}}{k}\right) \pm \sqrt{\left(\gamma k + \frac{R_{1D}}{k}\right)^2 + 4\frac{L_{1D}}{C_{1D}}}}{2L_{1D}}. \quad (18)$$

Solving Equation (17) for  $k$  leads to

$$k^2 = \xi e^{I(\theta + 2n\pi)}, \quad (19)$$

where  $n$  is an integer number and

$$\xi = \frac{\omega C_{1D}}{1 + (\gamma \omega C_{1D})^2} \sqrt{\omega^2 (L_{1D} - \gamma C_{1D} R_{1D})^2 + (R_{1D} + \gamma \omega^2 C_{1D} L_{1D})^2},$$

$$\theta = \arctan\left(\frac{-R_{1D} - \gamma \omega^2 C_{1D} L_{1D}}{\omega (L_{1D} - \gamma C_{1D} R_{1D})}\right).$$

Substitution of Equations (16) into the first equation in (14) yields

$$\widehat{q} = c_p C_{1D} \widehat{p}_e. \quad (20)$$

---

<sup>2</sup>We will focus on the solution for waves travelling in the positive  $x$ -direction. An identical analysis with  $p_e = \widehat{p}_e e^{I(\omega t + kx)}$  and  $q = \widehat{q} e^{I(\omega t + kx)}$  provides the solution for waves travelling in the negative  $x$ -direction.

Assuming that  $\widehat{p}_e$  is real,  $\widehat{q}$  must be complex because  $c_p$  is complex. We can write  $\widehat{q} = \Re(\widehat{q}) + I\Im(\widehat{q})$ , where  $\Re$  and  $\Im$  denote the real and imaginary parts of  $\widehat{q}$ , respectively. Therefore, Equations (16) become

$$p_e(x, t) = \widehat{p}_e e^{\Im(k)x} e^{I(\omega t - \Re(k)x)}, \quad (21a)$$

$$q(x, t) = \left( \Re(\widehat{q}) + I\Im(\widehat{q}) \right) e^{\Im(k)x} e^{I(\omega t - \Re(k)x)}. \quad (21b)$$

The physical solution to System (14) is the real part of  $p_e$  and  $q$  in (21), which takes the form

$$\Re(p_e) = \widehat{p}_e e^{\Im(k)x} \cos(\omega t - \Re(k)x), \quad (22a)$$

$$\Re(q) = e^{\Im(k)x} \left( \Re(\widehat{q}) \cos(\omega t - \Re(k)x) - \Im(\widehat{q}) \sin(\omega t - \Re(k)x) \right). \quad (22b)$$

Equations (18), (19) and (22) allow us to study the individual roles of  $R_{1D}$ ,  $L_{1D}$ ,  $C_{1D}$ ,  $\gamma$  and  $\omega$  into the shape of the pressure and flow pulse waves before any reflection. In the cardiovascular system and under normal conditions  $R_{1D} > 0$ ,  $L_{1D} > 0$ ,  $C_{1D} > 0$ , and  $\gamma > 0$ . Therefore, assuming  $\omega > 0$  (i.e. we are interested in unsteady solutions),

$$\Im(k^2) = -\frac{\omega C_{1D}}{1 + (\gamma \omega C_{1D})^2} (R_{1D} + \gamma \omega^2 C_{1D} L_{1D}) < 0.$$

Moreover

$$\Re(k^2) = \frac{\omega^2 C_{1D}}{1 + (\gamma \omega C_{1D})^2} (L_{1D} - \gamma C_{1D} R_{1D}) > 0$$

and  $-\pi/2 < \theta < 0$ , whenever  $L_{1D} > \gamma C_{1D} R_{1D}$ , which is equivalent to

$$\rho h E > \frac{3}{2} (\zeta + 2) \tilde{\gamma} \mu, \quad (23)$$

where we used  $\gamma = \tilde{\gamma}/2\sqrt{\pi A_0}$ . Using the data shown in Table 2 for the human aorta, we have that  $\rho h E$  is an order of magnitude greater than  $\frac{3}{2}(\zeta + 2)\tilde{\gamma}\mu$ . Therefore,  $k = \sqrt{\xi} e^{I(\theta/2 + n\pi)}$  satisfies  $-\pi/4 < \theta < 0$ ,  $\Re(k) > 0$  and  $\Im(k) < 0$ .

Equations (22) show that  $\Im(k)$  modulates the amplitude of the pressure and flow waves, which decay exponentially with  $x$  when  $\Im(k) < 0$ . Moreover the absolute value of  $\Im(k)$  is monotonically increasing with respect to the frequency  $\omega$ . If we consider its dependence on the problem parameters, it increases with  $\mu$  and  $\gamma$ , while it decreases with the Young's modulus  $E$ .

If we assume that the fluid is inviscid ( $R_{1D} = 0$ ) and the arterial wall is purely elastic ( $\tilde{\gamma} = 0$ ), Equations (17) and (18) reduce to  $k = \omega\sqrt{L_{1D}C_{1D}}$  and

$$c_p = \tilde{c}_i = 1/\sqrt{L_{1D}C_{1D}}, \quad (24)$$

so that  $\Im(k) = 0$ ,  $\Im(\widehat{q}) = 0$ , and Equations (22) become

$$p = p_e = \widehat{p}_e \cos(\omega t - kx), \quad (25a)$$

$$q = \widehat{q} \cos(\omega t - kx). \quad (25b)$$

Property	Value
Cross-sectional area $A_0$	$\pi \text{ cm}^2$
Wall thickness $h$	1.5 mm
Blood mass density $\rho$	1050 Kg m <sup>-3</sup>
Blood viscosity $\mu$	4 mPa s
Velocity profile constant $\zeta$	9
Young's modulus $E$	0.4 MPa
Voigt-type viscous modulus $\tilde{\gamma}$	0.3 MPa s m <sup>-1</sup>

Table 2: Typical geometrical and mechanical properties of the human aorta based on [10, 12, 35, 42]. The resulting linear inviscid pulse wave speed is  $\tilde{c}_i = 6.17 \text{ m s}^{-1}$ .

Equations (24) and (25) indicate that pressure and flow are in phase, have a constant amplitude, and travel with a frequency-independent speed  $\tilde{c}_i$ . If either  $\tilde{\gamma} > 0$  or  $R_{1D} > 0$ , pressure and flow are not in phase and their amplitudes decrease exponentially with the axial distance  $x$  as dictated by  $\Im(k)$ . Moreover,  $c_p$  depends on  $k$  and, hence, both the viscosity of the fluid and the wall cause wave dispersion (i.e. higher-frequency waves travel faster than lower-frequency waves).

### 2.3.2 Global effects

Based on the analysis presented in [7] for the elastic wall case, we integrate the first two equations in (14) along the length  $l$  of an arterial segment in which  $x \in [0, l]$  to obtain

$$\begin{cases} C_{0D} \frac{d\tilde{p}_e}{dt} + q_{out} - q_{in} = 0, \\ L_{0D} \frac{d\tilde{q}}{dt} + p_{e_{out}} - p_{e_{in}} - \gamma \left( \frac{\partial q_{out}}{\partial x} - \frac{\partial q_{in}}{\partial x} \right) = -R_{0D}\tilde{q}, \end{cases} \quad (26)$$

where  $q_{in}(t) = q(0, t)$ ,  $q_{out}(t) = q(l, t)$ ,  $\partial q_{in}/\partial x(t) = \partial q/\partial x(0, t)$ ,  $\partial q_{out}/\partial x(t) = \partial q/\partial x(l, t)$ ,  $p_{e_{in}}(t) = p_e(0, t)$ ,  $p_{e_{out}}(t) = p_e(l, t)$ ,  $R_{0D} = R_{1D}l$ ,  $L_{0D} = L_{1D}l$ ,  $C_{0D} = C_{1D}l$ , and

$$\tilde{p}_e(t) = \frac{1}{l} \int_0^l p_e dx, \quad \tilde{q}(t) = \frac{1}{l} \int_0^l q dx,$$

which represent the elastic mean pressure and flow rate over the whole segment.

Equation (26) applies to each segment of a bifurcating tree arterial net-

work with  $N + 1$  segments and  $M$  outflows ( $M < N + 1$ ); i.e.

$$\begin{cases} C_{0D}^i \frac{d\tilde{p}_e^i}{dt} + q_{out}^i - q_{in}^i = 0, \\ L_{0D}^i \frac{d\tilde{q}^i}{dt} + p_{e_{out}}^i - p_{e_{in}}^i - \gamma^i \left( \frac{\partial q_{out}^i}{\partial x} - \frac{\partial q_{in}^i}{\partial x} \right) = -R_{0D}^i \tilde{q}^i, \end{cases} \quad i = 0, \dots, N, \quad (27)$$

where the superscript  $i$  indicates the number of the segment. For the sake of simplicity we assume that segments numbered from 0 to  $M$  have one end that interfaces with the rest of the circulatory system. In particular, the inflow  $q_{in}^0$  at the proximal end of Segment 0 (the ascending aorta) is prescribed to be equal to the cardiac ejection  $q_{IN}(t)$ . As for vessels numbered from 1 to  $M$ , the distal end interfaces with the peripheral circulation.

Enforcing conservation of mass at the junctions of the network, the  $N + 1$  equations of conservation of mass in (27) combine to produce

$$q_{IN} = \sum_{j=1}^M q_{out}^j + \sum_{i=0}^N C_{0D}^i \frac{d\tilde{p}_e^i}{dt}. \quad (28)$$

It is well known that the peripheral resistance is much greater than the resistance in larger arteries [12, Chap. 12]. Therefore, for the purpose of studying the global circulation, we can assume  $R_{0D}^i = 0$ ,  $i = 0, \dots, N$ .

Next we will explore the implications of time-averaging Equation (28) and taking  $L_{0D}^i = 0$ ,  $i = 0, \dots, N$ , in (27).

**Time-averaged behaviour.** Integrating Equation (28) over a cardiac cycle  $T_0 \leq t \leq T_f$  yields

$$T \left( \bar{q}_{IN} - \sum_{j=1}^M \bar{q}_{out}^j \right) = \sum_{i=0}^N C_{0D}^i [\tilde{p}_e^i(T_f) - \tilde{p}_e^i(T_0)], \quad (29)$$

where

$$\bar{q}_{IN} = \frac{1}{T} \int_{T_0}^{T_f} q_{IN} dt, \quad \bar{q}_{out}^j = \frac{1}{T} \int_{T_0}^{T_f} q_{out}^j dt$$

are the mean values of  $q_{IN}$  (cardiac output) and  $q_{out}^j$ ,  $j = 1, \dots, M$ , over the interval  $[T_0, T_f]$ , respectively, and  $T = T_f - T_0$  is the period of the heartbeat. If each terminal segment is coupled to a matched RCR windkessel model relating  $q_{out}^j$  to  $p_{e_{out}}^j$ ,  $j = 1, \dots, M$ , (Figure 2) through [7]

$$q_{out}^j \left( 1 + \frac{Z_0^j}{R_j} \right) + C_j Z_0^j \frac{dq_{out}^j}{dt} = \frac{p_{e_{out}}^j - P_{out}}{R_j} + C_j \frac{dp_{e_{out}}^j}{dt}, \quad (30)$$

with a constant peripheral resistance  $R_j$ , compliance  $C_j$ , characteristic impedance  $Z_0^j = \rho/A_0^j \sqrt{L_{0D}^j C_{0D}^j}$  and outflow pressure  $P_{out}$ , and the flow is assumed to

be periodic with a period  $T$ , then the total peripheral outflow takes the form

$$\bar{q}_{IN} = \sum_{j=1}^M \bar{q}_{out}^j = \sum_{j=1}^M \frac{\frac{1}{T} \int_{T_0}^{T_f} p_{e_{out}}^j dt - P_{out}}{R_j + Z_0^j}. \quad (31)$$

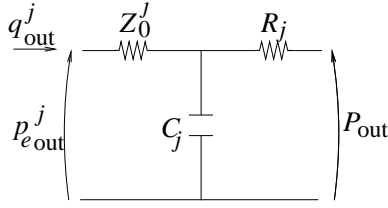


Figure 2: The  $j$ -th terminal segment of the arterial network,  $j = 1, \dots, M$ , is coupled to an RCR windkessel model relating the outgoing flow  $q_{out}^j$  to the pressure  $p_{e_{out}}^j$ . The downstream vasculature is represented by a constant peripheral resistance  $R_j$ , compliance  $C_j$ , characteristic impedance  $Z_0^j$  and outflow pressure  $P_{out}$ .

Integrating the balance of momentum in Equation (27) over the same cardiac cycle  $T_0 \leq t \leq T_f$  and assuming periodic flow with a period  $T$  leads to

$$\int_{T_0}^{T_f} p_{e_{out}}^i dt - \int_{T_0}^{T_f} p_{e_{in}}^i dt = \int_{T_0}^{T_f} \gamma^i \left( \frac{\partial q_{out}^i}{\partial x} - \frac{\partial q_{in}^i}{\partial x} \right) dt = \int_{T_0}^{T_f} \gamma^i \left( \frac{\partial a_{in}^i}{\partial t} - \frac{\partial a_{out}^i}{\partial t} \right) dt = 0, \quad i = 0, \dots, N, \quad (32)$$

where  $\partial a_{in}/\partial t(t) = \partial a/\partial t(0, t)$  and  $\partial a_{out}/\partial t(t) = \partial a/\partial t(l, t)$ . Since Equation (27) holds for any length  $l$ , we deduce that  $\int_{T_0}^{T_f} p_{e_{out}}^i dt = \int_{T_0}^{T_f} p_{e_{in}}^i dt = \int_{T_0}^{T_f} p_e^i dt$ ,  $i = 0, \dots, N$ ,  $p_e^i$  being evaluated in any location of the  $i$ -th arterial segment. Moreover, the tube law in (14) allows us to write  $\int_{T_0}^{T_f} p_e^i dt = \int_{T_0}^{T_f} p^i dt$ ,  $i = 0, \dots, N$ , since  $\int_{T_0}^{T_f} \frac{\partial q^i}{\partial x} dt = - \int_{T_0}^{T_f} \frac{\partial a^i}{\partial t} dt = 0$ ,  $i = 0, \dots, N$ . Combining these results with continuity of pressure at the junctions of the network reduces Equation (31) to

$$\bar{q}_{IN} = \sum_{j=1}^M \bar{q}_{out}^j = \frac{\bar{p}_w - P_{out}}{R_T}, \quad (33)$$

where

$$\frac{1}{R_T} = \sum_{j=1}^M \frac{1}{R_j + Z_0^j}, \quad \bar{p}_w = \frac{1}{T} \int_{T_0}^{T_f} p_e^j dt = \frac{1}{T} \int_{T_0}^{T_f} p(x, t) dt, \quad j = 0, \dots, M,$$

are the total peripheral resistance and space-independent mean pressure, respectively, of the network.

Equation (33) shows that the cardiac output and total peripheral resistance dictate the mean pressure  $\bar{p}_w$  that perfuses the microcirculation. Equation (29) shows that the elastic wall compliance and period of the heart beat determine the time it takes to have  $\tilde{p}_e^i(T_f) = \tilde{p}_e^i(T_0)$  ( $i = 0, \dots, N$ ) and  $\bar{q}_{IN} = \sum_{j=1}^M \bar{q}_{out}^j$ , and hence reach a periodic state in which Equation (33) is satisfied.

**Neglecting blood inertial effects.** Taking  $L_{0D}^i = 0$ ,  $i = 0, \dots, N$ , reduces the  $N + 1$  equations of balance of momentum in (27) to

$$p_{e_{in}}^i - \gamma^i \frac{\partial q_{in}^i}{\partial x} = p_{e_{out}}^i - \gamma^i \frac{\partial q_{out}^i}{\partial x}, \quad i = 0, \dots, N; \quad (34)$$

i.e. the total pressure  $p = p_e - \gamma \frac{\partial q}{\partial x}$  is the same at the inlet and outlet of each segment. Furthermore  $\frac{\partial q_{in}^i}{\partial x} = \frac{\partial q_{out}^i}{\partial x}$ ,  $i = 0, \dots, N$ , since the  $N + 1$  equations of conservation of mass in (27) require  $q_{out}^i - q_{in}^i = -C_{0D}^i \frac{d\tilde{p}_e^i}{dt}$ ,  $i = 0, \dots, N$ , so that  $\frac{\partial q_{out}^i}{\partial x} - \frac{\partial q_{in}^i}{\partial x} = 0$ ,  $i = 0, \dots, N$ . Consequently we have  $p_{e_{in}}^i = p_{e_{out}}^i$ ,  $i = 0, \dots, N$ . Moreover,

$$p_{e_{in}}^i = p_{e_{out}}^i = \tilde{p}_e^i, \quad \gamma^i \frac{\partial q_{out}^i}{\partial x} = \gamma^i \frac{\partial q_{in}^i}{\partial x} = \gamma^i \left( \frac{\partial q}{\partial x} \right)^i, \quad i = 0, \dots, N, \quad (35)$$

in any location of the  $i$ -th arterial segment, because Equation (27) holds for any length  $l$ .

Assuming continuity of elastic pressure at the junctions of the bifurcating tree arterial network (which is in agreement with the boundary conditions considered in both the TG and DG schemes), we obtain  $\tilde{p}_e^i = p_w$ ,  $i = 0, \dots, N$ , where  $p_w(t)$  is the space-independent pressure to which the 1-D model elastic pressures in (14) approach when  $R_{0D}^i = 0$  and  $L_{0D}^i \rightarrow 0$ ,  $i = 0, \dots, N$ . Equation (28) becomes

$$q_{IN} = \sum_{j=1}^M q_{out}^j + C_c \frac{dp_w}{dt}, \quad (36)$$

where  $C_c = \sum_{i=0}^N C_{0D}^i$  is the total conduit compliance.

If each terminal segment is coupled to the matched RCR windkessel model governed by Equation (30), with  $p_{e_{out}}^j = p_w$ ,  $j = 1, \dots, M$ , when  $R_{0D}^i = 0$  and  $L_{0D}^i = 0$ ,  $i = 0, \dots, N$ , then Equation (36) yields

$$q_{IN} = q_{OUT} + C_T \frac{dp_w}{dt}, \quad (37)$$

$$q_{OUT} = \frac{p_w - P_{out}}{R_T} - \sum_{j=1}^M \frac{C_j Z_0^j R_j}{R_j + Z_0^j} \frac{dq_{out}^j}{dt},$$

$$C_T = C_c + C_p, \quad C_p = \sum_{j=1}^M \frac{R_j C_j}{R_j + Z_0^j},$$

where  $q_{OUT}(t)$  is the total outflow through the terminal segments of the system,  $C_T$  is the total compliance, and  $C_p$  is the total peripheral compliance. The solution to Equation (37) is

$$p_w = P_{out} + (p_w^0 - P_{out})e^{\frac{T_0-t}{R_T C_T}} + e^{\frac{-t}{R_T C_T}} \int_{T_0}^t \left( q_{IN}(t') + \sum_{j=1}^M \frac{C_j Z_0^j R_j}{R_j + Z_0^j} \frac{dq_{out}^j(t')}{dt'} \right) e^{\frac{t'}{R_T C_T}} dt', \quad t \geq T_0, \quad (38)$$

where  $p_w^0 = p_w(T_0)$  is the pressure  $p_w$  at the reference time  $t = T_0$ .

In [7] we showed that diastolic pressures for a purely elastic model of the largest 55 conduit arteries in the human tend to the space-independent pressure  $p_w$  determined by Equation (38), which depends on global quantities: the cardiac ejection, total compliance, total peripheral resistance and outflow pressure. This implies  $L_{0D}^i \rightarrow 0$ ,  $i = 0, \dots, N$  during diastole. Indeed, *in vivo* data in normal conditions shows that pressure waveforms are approximately space-independent in about the last two thirds of diastole [1, 41]. According to this visco-elastic analysis, only the elastic component of pressure in each arterial segment,  $p_e^i$ ,  $i = 0, \dots, N$ , tends to  $p_w$  during diastole, whereas the total pressure  $p^i$  tends to  $p_w + \gamma^i \left( \frac{\partial q}{\partial x} \right)^i$ ,  $i = 0, \dots, N$ , in which  $\gamma^i$  and  $\left( \frac{\partial q}{\partial x} \right)^i$  are, in general, different in each arterial segment. Note that despite  $q_{IN} = 0$  during normal diastolic conditions, the cardiac ejection also affects  $p_w$ , because  $p_w^0$  depends on  $q_{IN}$  earlier in the cardiac cycle.

It is interesting to remark that if  $C_j = 0$  ( $j = 1, \dots, M$ ) in Equation (30) (i.e. each terminal segment is coupled to a terminal resistance  $R_j + Z_0^j$ ), then the lumped parameter model described by Equation (36) becomes the windkessel equation proposed by Frank [19],

$$q_{IN} = \frac{p_w - P_{out}}{R_T} + C_c \frac{dp_w}{dt}. \quad (39)$$

## 2.4 Local viscous modulus and compliance estimation from simultaneous pressure and diameter measurements

Given simultaneous measurements of pressure  $P(t)$  and diameter  $D(t)$  at an arbitrary location in the arterial network,  $\gamma$  can be estimated as

$$\gamma = \frac{\int_{A(T_0)}^{A(T_f)} P dA}{\int_{A(T_0)}^{A(T_f)} \frac{\partial A}{\partial t} dA}, \quad A = \pi D^2/4, \quad (40)$$

assuming a circular cross section and a periodic flow with a period  $T = T_f - T_0$ , so that  $A(T_0) = A(T_f)$ .

Our numerical results will show that  $\frac{\partial A}{\partial t}$  is approximately constant during the last part of diastole. Therefore  $\gamma \frac{\partial q}{\partial x} = -\gamma \frac{\partial a}{\partial t}$  is also approximately constant in the linear elastic tube law (14), so that the relation between  $p$  and  $a$  is approximately proportional to  $C_{1D}$  and can be directly estimated if simultaneous pressure and diameter measurements are available. Once  $C_{1D}$  is known, we can then calculate the inviscid pulse wave speed  $\tilde{c}_i$  using Equation (24), with  $L_{1D}$  obtained from Equation (15) taking  $A_0$  to be the diastolic (minimum) area of the diameter measurement.

### 3 Results and discussion

The TG and DG formulations described in Sections 2.2.1 and 2.2.2 converge to the analytical pressure and flow waveforms in Figure 3, which are given by Equations (22) in an artery with the geometrical and mechanical properties shown in Table 2 and with boundaries at  $x = 0$  and  $x = 10$  m. The DG scheme was run with 10 elements, a polynomial and quadrature order of 3, and a time step  $\Delta t = 0.01$  s. The TG scheme was run using a piecewise linear approximation with a grid size  $h = 20$  cm (50 elements) and the same time step. A non-physiological length of 10 m was considered to highlight the exponential damping of the pulse wave caused by the viscosity of the wall and the fluid. A small amplitude pressure wave was propagated to minimise the effect of the nonlinear terms in Equations (7) and (8) (which cannot be appreciated in the scale of Figure 3), so that the numerical results can be compared against their analytical counterparts.

The outcomes of the linear analysis on the local and global effects of physical properties on pulse wave propagation are illustrated using a single-artery model of the human aorta (Section 3.1) and the model of the human cerebral circulation in Figure 1 (Section 3.2) under normal physiological conditions. All the numerical results shown in this work were obtained using both formulations, which converged to the same results (their differences cannot be distinguished in the scales of Figures 4 and 6 to 10).

#### 3.1 Wave propagation in a single vessel

The relative importance of wall and fluid viscosity on pressure damping varies with the frequency  $\omega$ . At lower frequencies fluid-viscosity damping is dominant (Figure 3, top), whereas at higher frequencies wall-viscosity damping is dominant (Figure 3, bottom). The flow waveform also presents this frequency-dependent behaviour, but with a phase difference from the pressure waveform that depends on  $\Im(\hat{q})$ , as shown by Equation (22b).

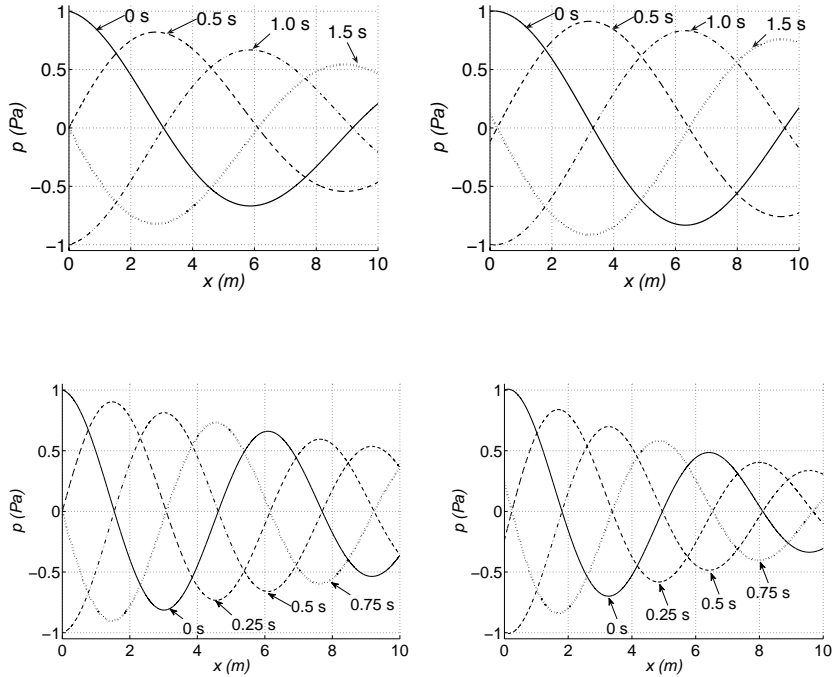


Figure 3: Pressure with distance at the times indicated by the labels in a 10 m long vessel with the properties shown in Table 2, assuming  $\tilde{\gamma} = 0$  (left) and  $\mu = 0$  (right). They are given by Equations (22) with  $\hat{p}_e = 1$  Pa and  $\omega = \pi$  s $^{-1}$  (top),  $\omega = 2\pi$  s $^{-1}$  (bottom).

### 3.1.1 Gaussian wave

Figure 4 compares the effects of fluid and wall viscosities using a narrow Gaussian-shaped wave propagated from the inlet of the same single vessel, but with  $\tilde{\gamma} = 10^4$  Pa s m $^{-1}$  and the initial conditions  $A(x) = A_0$  and  $Q(x) = 0$ . This wave is a continuous approximation to the unit pulse  $\delta(t-t_0)$ ,  $t_0 = 0.05$  s (i.e.  $\delta(t_0) = 1$  and  $\delta(t) = 0$  for  $t \neq t_0$ ) and hence contains multiple excitation frequencies. A smaller  $\tilde{\gamma}$  is considered here because the dependence of  $\Im(k)$  on  $\omega$  (see Equation (19)) leads to a larger dissipation of the Gaussian inflow, since it features higher frequencies than the sinusoidal waves considered previously. A completely absorbent outflow boundary condition is enforced; i.e. the terminal reflection coefficient, which is defined as the ratio of the change of pressure across the reflected wave to the change of pressure in the incident wave, is equal to zero. This is equivalent to a terminal resistance equal to the characteristic impedance of the vessel  $Z_0$  [6]. The DG scheme was run with 250 elements, a polynomial and quadrature order of 4, and a time step  $\Delta t = 100$   $\mu$ s. The TG scheme was run using a piecewise linear approximation with a grid size  $h = 0.5$  cm (2000 elements) and the same time step.

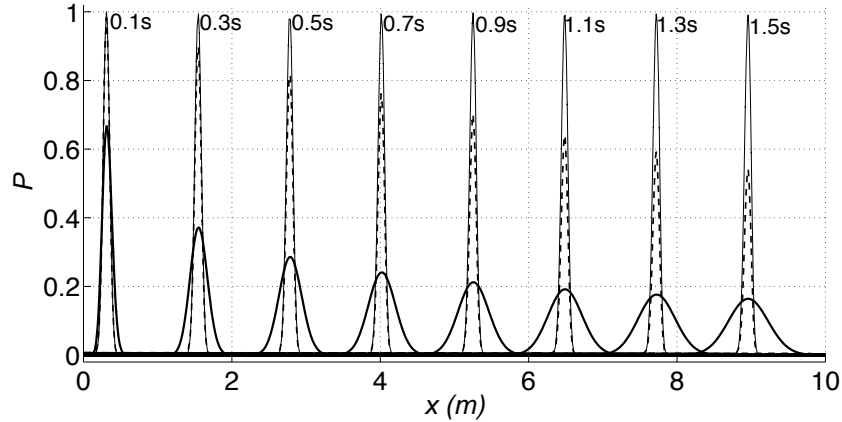


Figure 4: Pressure with distance at the times indicated by the labels produced by the propagation of a Gaussian-shaped wave from the inlet of a 10 m long vessel with an absorbent outlet and the properties shown in Table 2, except for  $\tilde{\gamma} = 10^4$  Pa s m<sup>-1</sup>. Three cases are considered: elastic wall and inviscid fluid (thin solid lines), visco-elastic wall and inviscid fluid (thick solid lines), and elastic wall and viscous fluid (dashed lines). Pressures were non-dimensionalised by the peak value of the inflow Gaussian wave.

As predicted by the analytical solution, wall viscosity produces a more significant pressure damping than does fluid viscosity, since high frequencies are dominant in the Gaussian wave considered. Moreover, as opposed to fluid viscosity, wall viscosity widens the foot of the wave as it propagates, which can be explained using our analytical solution. Solving Equation (18) for  $\omega \in (0, 100]$  and  $\tilde{\gamma} = 0$  shows that fluid viscosity causes wave dispersion mainly at low frequencies, with  $|c_p| \rightarrow \tilde{c}_i$  and the phase angle of  $c_p$  tending to zero with the increasing  $\omega$  (Figure 5, left). On the other hand, solving Equation (18) for  $\omega \in (0, 100]$  and  $\mu = 0$  shows that the wave dispersion due to wall viscosity increases with the increasing  $\omega$ ;  $|c_p| - \tilde{c}_i$  and the phase angle of  $c_p$  increase with the increasing  $\omega$  (Figure 5, right). As indicated by Equations (22), viscous pressure and flow are out of phase with a phase difference that depends on frequency, this difference being larger for the case with visco-elastic wall and inviscid fluid.

Propagation of the unit pulse  $\delta$  in a linear dynamic system produces the so called impulse response function, whose convolution with any input function yields its corresponding output function directly in the time domain [24]. Thus, the pressure waveforms shown in Figure 4 are continuous approximations to the impulse response functions at different times. When nonlinear effects are small (as it is the case for arterial pulse wave propagation in normal conditions [25]), the shape of the waves in Figure 4 can be used to show that fluid viscosity only decreases the magnitude of the pulse waveform with distance, whereas wall viscosity also modifies its shape, specially when high

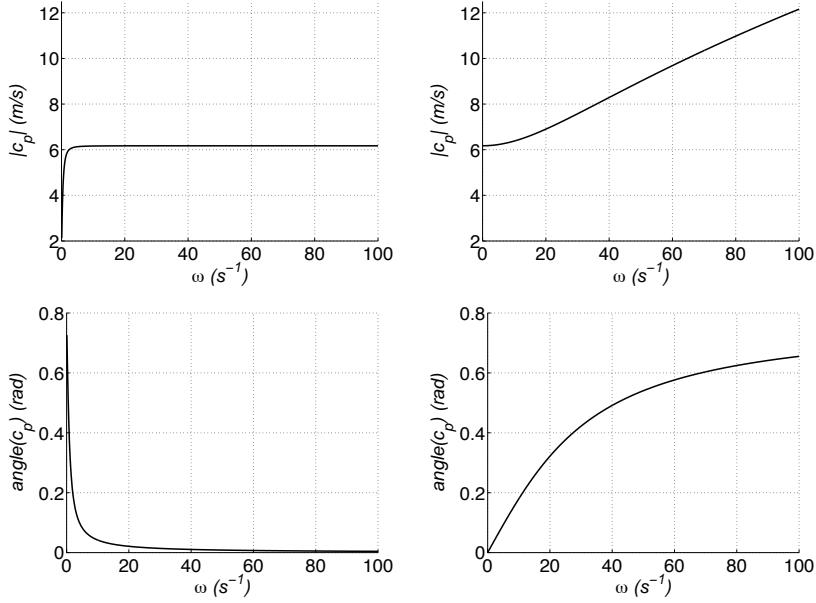


Figure 5: Modulus (top) and phase angle (bottom) of the phase velocity  $c_p$  with  $\omega$  in the vessel with the properties shown in Table 2, assuming  $\tilde{\gamma} = 0$  (left) and  $\mu = 0$  (right).

frequencies are dominant in the inflow wave.

### 3.1.2 Half-sine wave

Next, we study the propagation of a periodic half-sinusoidal flow wave (Figure 6, right), which approximates the outflow from the left ventricle in normal conditions, from the inlet of a visco-elastic vessel with inviscid flow and the properties shown in Table 2. The vessel has a length of 40 cm (which is normal for the human aorta) and its outlet is coupled to an RCR windkessel model with a terminal resistance  $R + Z_0 = 189 \text{ MPa s m}^{-3}$ , a terminal compliance  $C = 6.3 \text{ m}^3 \text{ GPa}^{-1}$ , and an outflow pressure  $P_{out} = 1.33 \text{ kPa}$  [6]. The DG scheme was run with 8 elements, a polynomial and quadrature order of 4, and a time step  $\Delta t = 100 \mu\text{s}$  for the purely elastic case and  $\Delta t = 50 \mu\text{s}$  for the visco-elastic case. The TG scheme was run using a piecewise linear approximation with a grid size  $h = 0.5 \text{ cm}$  (80 elements) and  $\Delta t = 100 \mu\text{s}$  in both cases.

Figure 6 (left and right) shows that, once a periodic state is reached, wall viscosity smoothes the elastic pressure ( $P_e$ ) and flow waveforms predominantly where high frequencies are dominant. During early systole, the expansion of the vessel wall ( $\partial A / \partial t > 0$ ) leads to a larger pressure in the visco-elastic vessel than in the purely elastic vessel (Figure 6, left), which is in agreement with Equation (6). The opposite effect is observed when the

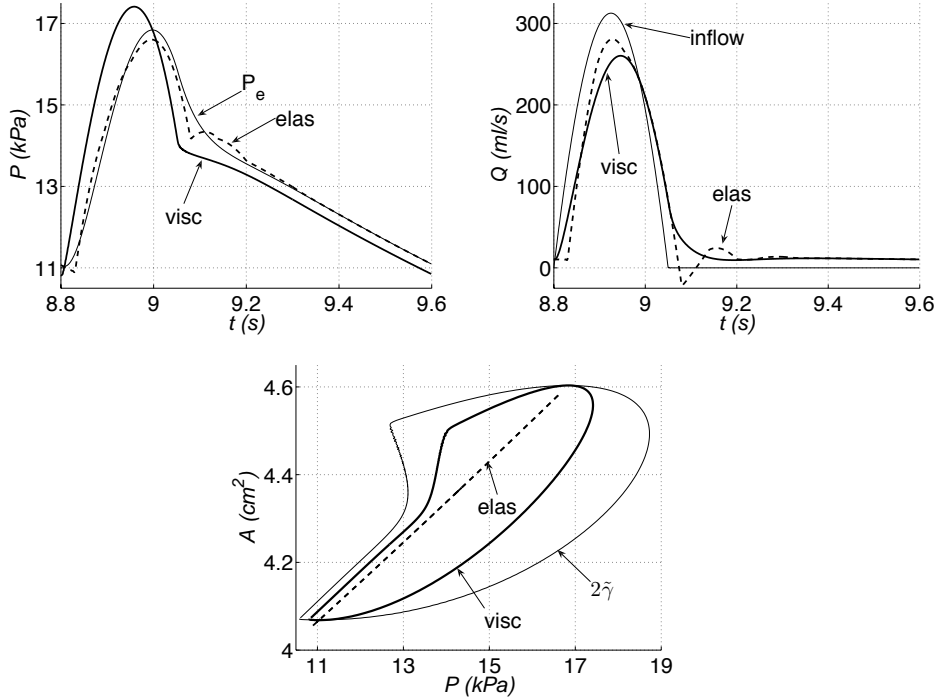


Figure 6: Pressure (left) and flow rate (right) time histories, and area-pressure curve (bottom) in the midpoint of a 40 cm long vessel with the properties shown in Table 2 once a periodic state is reached. A periodic half-sinusoidal flow wave was prescribed at the inlet (inflow) and the outlet was coupled to an RCR windkessel model. Two inviscid-flow cases are shown: elastic wall (elas) and visco-elastic wall (visc). For the visco-elastic case, the left panel shows the elastic pressure  $P_e$  and the bottom panel a case with  $\tilde{\gamma} = 0.6 \text{ MPa s m}^{-1}$  ( $2\tilde{\gamma}$ ).

vessel wall relaxes ( $\partial A/\partial t < 0$ ) in diastole and late systole. Moreover, the foot of the pulse wave, which is made of higher frequencies than the rest of the waveform, arrives at the measuring site earlier in the visco-elastic model than in the purely elastic model, in agreement with the increase in wave dispersion with frequency shown in Figure 5 (right). Mean pressures remain unchanged throughout the vessel, as predicted by Equation (33) since  $\bar{q}_{IN}$ ,  $P_{out}$  and  $R_T = R + Z_0$  are constant.

Fluid viscosity increases the mean pressure in the middle of the vessel (by about 20 Pa) without affecting the shape of the pressure wave, but this feature cannot be distinguished in the scale of Figure 6 (left) from the inviscid-flow cases. Similarly, fluid viscosity does not change the shape of the flow wave; differences between the viscous and inviscid-flow cases cannot be distinguished in the scale of Figure 6 (right). The mean flow rates are maintained constant throughout the vessel for all the cases studied, since conservation of mass in System (1) is not affected by fluid or wall viscosity.

The  $A$ - $P$  curves obtained for the visco-elastic case present hysteresis, with the pressure range increasing with  $\tilde{\gamma}$  and the area range remaining constant (Figure 6, bottom). The curves evolve in time counterclockwise, showing a different behaviour during loading and unloading. Application of Equation (40) and taking  $A_0$  to be the diastolic area yields  $\tilde{\gamma} = 2\sqrt{\pi A_0}\gamma = 0.344 \text{ MPa s m}^{-1}$  and  $\tilde{\gamma} = 0.685 \text{ MPa s m}^{-1}$  as the approximated values to  $\tilde{\gamma} = 0.3$  and  $0.6 \text{ MPa s m}^{-1}$ , respectively. The error between estimated and real  $\tilde{\gamma}$  is due to the error in the estimation of  $A_0$ .

During approximately the last three fourths of diastole, the relation between  $A$  and  $P$  is approximately linear and takes the slope of the elastic-wall case, which indicates that  $\gamma \frac{\partial A}{\partial t}$  is approximately constant in Equation (6). The same result is obtained at any location in the vessel, which is in agreement with  $\gamma \frac{\partial q}{\partial x}$  being space-independent in diastole, when  $L_{0D} \simeq 0$ , as was shown in Section 2.3.2. Following the method described in Section 2.4 to estimate the the inviscid pulse wave speed  $\tilde{c}_i$ , with  $A_0$  taken to be the diastolic (minimum) area in Figure 6 (bottom), we obtain  $\tilde{c}_i = 6.52 \text{ m/s}$  for  $\tilde{\gamma} = 0.3 \text{ MPa s m}^{-1}$  and  $\tilde{c}_i = 6.45 \text{ m/s}$  for  $\tilde{\gamma} = 0.6 \text{ MPa s m}^{-1}$ , which are a better approximation to the inviscid pulse wave speed  $\tilde{c}_i = 6.17 \text{ m/s}$  calculated using the parameters in Table 2 than that provided by current techniques based on simultaneous pressure and velocity measurements. The technique proposed in [23] using the linear part of the  $PU$ -loop yields  $\tilde{c}_i = 10.28 \text{ m/s}$  for  $\tilde{\gamma} = 0.3 \text{ MPa s m}^{-1}$  and  $\tilde{c}_i = 14.02 \text{ m/s}$  for  $\tilde{\gamma} = 0.6 \text{ MPa s m}^{-1}$ , whereas the sum-of-squares technique [15] yields  $\tilde{c}_i = 9.68 \text{ m/s}$  for  $\tilde{\gamma} = 0.3 \text{ MPa s m}^{-1}$  and  $\tilde{c}_i = 14.36 \text{ m/s}$  for  $\tilde{\gamma} = 0.6 \text{ MPa s m}^{-1}$ .

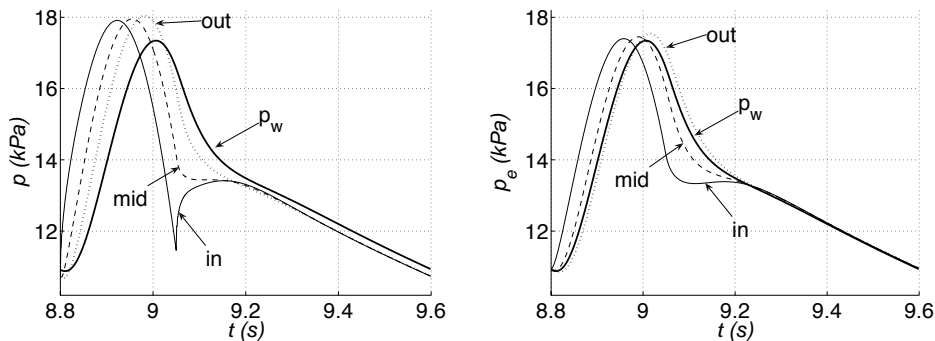


Figure 7: Total (left) and elastic (right) pressure time histories at the inlet (in), midpoint (mid) and outlet (out) of the inviscid-flow, visco-elastic aortic model considered in Figure 6. Nonlinearities were neglected to compare these pressures against the space-independent pressure  $p_w$  given by Equation (38).

When nonlinearities are neglected, the flow is assumed to be inviscid and the wall visco-elastic, pressures throughout the vessel tend to a space-independent shape during approximately the last three fourths of diastole (Figure 7). This shape is given by  $p_w$  (Equation (38)) for the elastic part

of pressure (Figure 7, right) and by  $p_w + \gamma \frac{\partial q}{\partial x}$  for the total pressure (Figure 7, left). The numerical results in Figure 7 were obtained by prescribing the inflow boundary condition in Figure 6 (right) scaled by 1000, so that nonlinearities could be assumed to be negligible, and then rescaling pressures under the assumption of linearity.

### 3.2 Wave propagation in the cerebral circulation

The effects of fluid and wall viscosity on the pulse waveforms shown for the aortic model are also present in the cerebral model (Figure 1 and Table 1). The DG scheme was run with a polynomial and quadrature order of 3, and a time step  $\Delta t = 5 \mu\text{s}$  for the elastic case and  $\Delta t = 1 \mu\text{s}$  for the visco-elastic case. The TG scheme was run using a piecewise linear approximation with a grid size  $h = 0.1 \text{ cm}$  in each domain and  $\Delta t = 10 \mu\text{s}$  in both cases.

Figure 8 compares pressure and velocity waveforms at three locations in the elastic and visco-elastic models (both with viscous fluid), showing that the visco-elastic damping effect is more significant for high pulse frequencies. The foot of the pulse wave arrives at any measuring site earlier in the visco-elastic wall case. The visco-elastic pressure is larger than the purely elastic pressure during most of systole and smaller during diastole. Mean pressures decrease as we move from the ascending aorta to more distal locations. Figure 9 shows, at two locations in the network, that the area-pressure curve presents hysteresis during systole and early diastole, and reduces to a line with the slope of the elastic-wall case during most of diastole.

Although the viscous modulus is  $\tilde{\gamma} = 0.3 \text{ MPa s m}^{-1}$  in all the arteries of the model (based on the data published in [10] for the carotid and femoral arteries of normotensive men) and  $\gamma$  increases with the decreasing  $A_0$  (Equation (5)), the visco-elastic effects shown in Figures 8 and 9 are more significant in larger arterial segments, because they have smaller inviscid pulse wave speeds and, hence, smaller Young's moduli. This result is in agreement with the increase in  $\Im(k)$  with the decreasing Young's modulus shown in Section 2.3.1.

When fluid viscosity is neglected along with the effect of nonlinearities, the elastic pressure waveform in any artery is well captured by  $p_w$  (Equation (38)) during most of diastole (Figure 10, right). In this numerical experiment, the inflow was prescribed to be equal to zero after  $t = 10 \text{ s}$ , to clearly exhibit the pressure trend in diastole. Figure 10 (left) shows that the total diastolic pressure tends to  $p_w + \gamma^i \left(\frac{\partial q}{\partial x}\right)^i$ ,  $i = 0, \dots, N$ , with  $\gamma^i \left(\frac{\partial q}{\partial x}\right)^i$  being constant within each arterial segment, as was predicted by the linear analysis in Section 2.3.2. According to this analysis, blood inertia is negligible when  $p_w$  is equal to the total pressure, which in our model occurs after approximately one fourth of diastole. This numerical result is in agreement with our single-artery findings in Figure 7 and with *in vivo* data measured

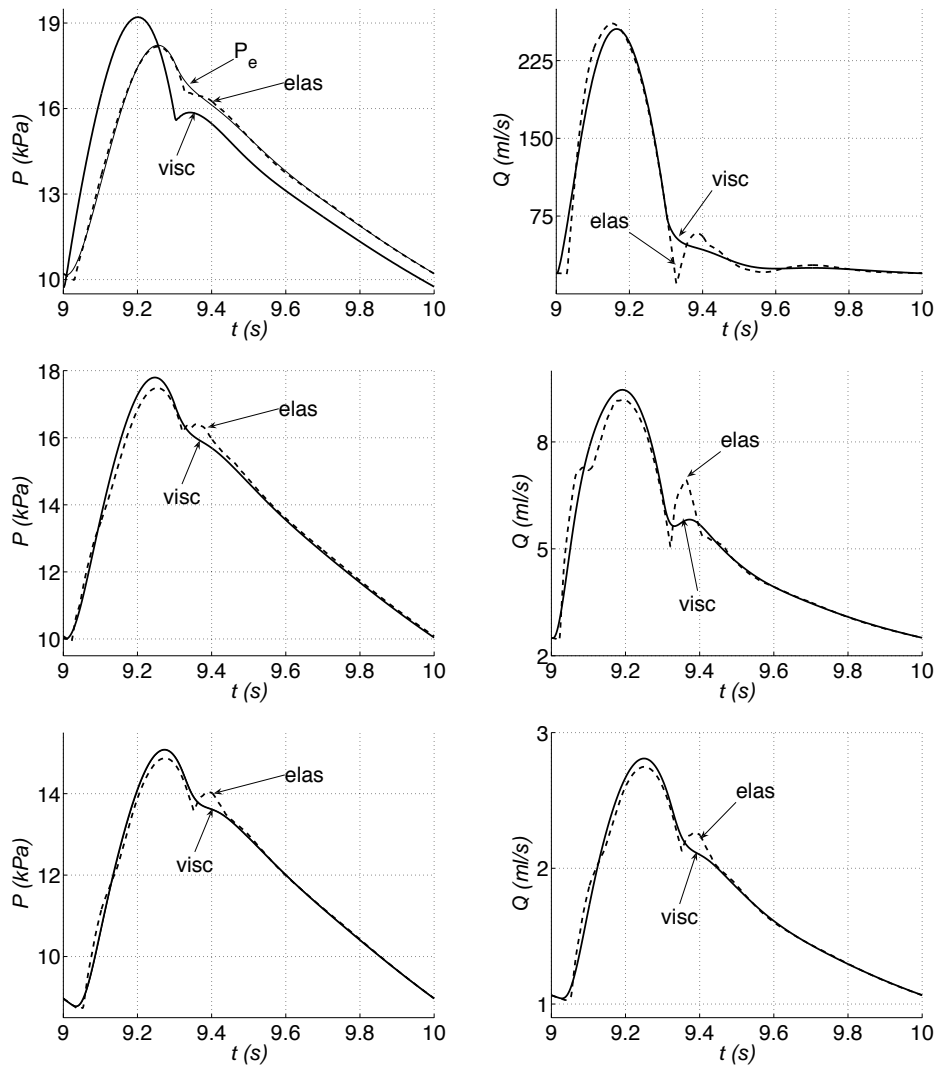


Figure 8: Pressure (left) and flow (right) time histories in the midpoint of the thoracic aorta (top), right carotid (middle) and left middle cerebral (bottom) arteries of the cerebral model (Figure 1), once a quasi-steady state is reached. Two fluid-viscous cases are shown: elastic wall (elas) and visco-elastic wall (visc). The left top panel also shows the elastic part of pressure  $P_e$ .

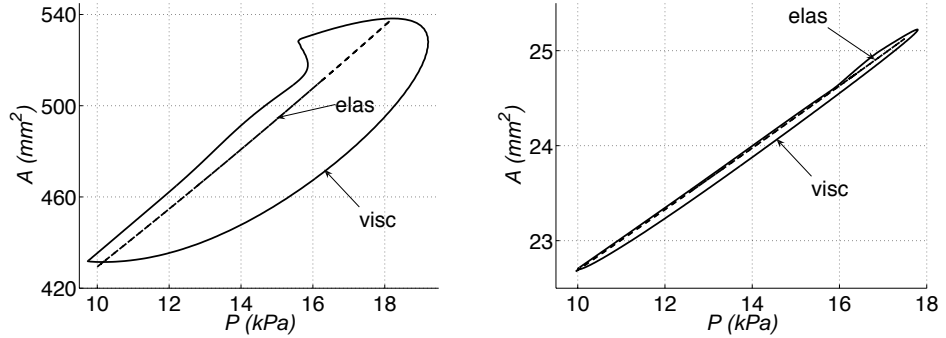


Figure 9: Area-pressure curves in the midpoint of the thoracic aorta (left) and right carotid artery (right) of the cerebral model (Figure 1), once a quasi-steady state is reached. Two fluid-viscous cases are shown: elastic wall (elas) and visco-elastic wall (visc).

at different locations in the human and canine aorta [1, 41]. Moreover, it suggests that the total resistance and compliance of the systemic circulation can be estimated from the time constant of the diastolic decay.

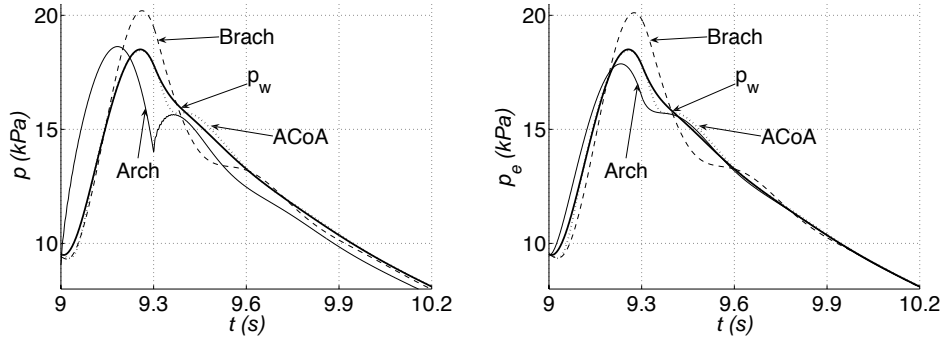


Figure 10: Total (left) and elastic (right) pressure time histories in the midpoint of the aortic arch I (Arch), left brachial (Brach) and anterior communicating artery (ACoA) of the inviscid-flow, visco-elastic cerebral model (Figure 1). Nonlinearities were neglected to compare these pressures against the space-independent pressure  $p_w$  given by Equation (38).

## 4 Conclusions

We have carried out an analytical and numerical study of the role of haemodynamic quantities into the typical shape of pressure and flow pulse waves in conduit arteries. Although we have focused on understanding the mechanisms underlying pulse wave propagation in the human aorta and cerebral circulation, the assumptions and conclusions of this study are valid in most

of the arterial conduit network; the coronaries being an exception due to the effect of myocardial contraction on pulse wave propagation, which was not considered in our study.

The numerical results have been verified by solving the nonlinear 1-D equations of pulse wave propagation in Voigt-type visco-elastic vessels using both a Taylor-Galerkin and a discontinuous Galerkin scheme, and cross-comparing the results. An additional verification has been made by comparing the numerical results to the analytical solution of pulse wave propagation in a linear, visco-elastic, single-artery model of the human aorta before any wave reflection.

According to our results, during systole and early diastole the pulse waveform is space and time dependent. Fluid and wall viscosities decrease the amplitude of pulse waves exponentially with distance; their damping effect increasing with the decreasing arterial stiffness. Fluid viscosity causes wave dispersion at lower frequencies, whereas wall viscosity increases wave dispersion with the increasing frequency of the pulse wave and causes hysteresis in the area-pressure curve. During approximately the last three fourths of diastole the inertial effects of the flow can be neglected, and pressures tend to a space-independent shape dictated by global quantities (cardiac ejection, total peripheral resistance and compliance, and outflow pressure) and the viscous modulus of each arterial segment. The cardiac output, total peripheral resistance and outflow pressure dictate the mean pressure that perfuses the microcirculation, and the period of the heart beat and wall compliance determine the time it takes to reach this mean pressure.

Information on the main haemodynamic quantities and mechanisms underlying pressure and flow pulse waveforms is important to identify those quantities that should be monitored to diagnose disease and conditions such as hypertension, and those that should be targeted to prevent and treat them. It also allows us to infer physical properties that are clinically relevant, such as local pulse wave speeds and viscous moduli, from simultaneous pressure and diameter measurements taken at the same location. According to our results, the area-pressure loop provides a more accurate estimation of local pulse wave speed than do current tools based on simultaneous pressure and velocity measurements [15, 23].

## Acknowledgments

This work was partially supported by a British-Italian partnership programme for young researchers (British Council/MIUR). Jordi Alastruey was also funded by a BHF Intermediate Basic Science Research Fellowship (FS/09/030/27812) and EPSRC Advanced Research Fellowship grant (EP/C539842/1) awarded to Professor Spencer Sherwin. Luca Formaggia gratefully acknowledges the support of MIUR through a PRIN07 grant.

## References

- [1] J. Aguado-Sierra, J. Alastruey, J.J. Wang, N. Hadjiloizou, J.E. Davies, and K.H. Parker. Separation of the reservoir and wave pressure and velocity from measurements at an arbitrary location in arteries. *Proc. Inst. Mech. Eng., Part H, J. Eng. Med.*, 222:403–416, 2008.
- [2] J. Alastruey. *Numerical modelling of pulse wave propagation in the cardiovascular system: development, validation and clinical applications*. Ph.D. thesis, Imperial College London, University of London, 2006.
- [3] J. Alastruey, S.R. Nagel, B. Nier, A.A.E Hunt, P.D. Weinberg, and J. Peiró. Modelling pulse wave propagation in the rabbit systemic circulation to assess the effects of altered nitric oxide synthesis. *J. Biomech.*, 42:2116–2123, 2009.
- [4] J. Alastruey, K.H. Parker, J. Peiró, S.M. Byrd, and S.J. Sherwin. Modelling the circle of Willis to assess the effects of anatomical variations and occlusions on cerebral flows. *J. Biomech.*, 40:1794–1805, 2007.
- [5] J. Alastruey, K.H. Parker, J. Peiró, and S.J. Sherwin. Can the modified Allen’s test always detect sufficient collateral flow in the hand? A computational study. *Comp. Meths. Biomech. Biomed. Eng.*, 9:353–361, 2006.
- [6] J. Alastruey, K.H. Parker, J. Peiró, and S.J. Sherwin. Lumped parameter outflow models for 1-D blood flow simulations: Effect on pulse waves and parameter estimation. *Commun. Comput. Phys.*, 4:317–336, 2008.
- [7] J. Alastruey, K.H. Parker, J. Peiró, and S.J. Sherwin. Analysing the pattern of pulse waves in arterial networks: a time-domain study. *J. Eng. Math.*, 64:331–351, 2009.
- [8] J. Alastruey, S.J. Sherwin, K.H. Parker, and D.D. Rubens. Placental transfusion insult in the predisposition for SIDS: A mathematical study. *Early Hum. Development*, 85:455–459, 2009.
- [9] R. Armentano, J. Barra, J. Levenson, A. Simon, and R.H. Pichel. Arterial wall mechanics in conscious dogs: Assessment of viscous, inertial, and elastic moduli to characterize aortic wall behavior. *Circulation Research*, 76:468–478, 1995.
- [10] R. Armentano, J.L. Megnien, A. Simon, F. Bellenfant, J. Barra, and J. Levenson. Effects of hypertension on viscoelasticity of carotid and femoral arteries in humans. *Hypertension*, 26:48–54, 1995.

- [11] D. Bessems, C.G. Giannopapa, M.C.M. Rutten, and F.N. van de Vosse. Experimental validation of a time-domain-based wave propagation model of blood flow in viscoelastic vessels. *J. Biomech.*, 41:284–291, 2008.
- [12] C.G. Caro, T.J. Pedley, R.C. Schroter, and W.A. Seed. *The mechanics of the circulation*. Oxford University Press, 1978.
- [13] B. Cockburn and C-W. Shu. The local discontinuous Galerkin method for time-dependent convection-diffusion systems. *SIAM J. Num. Anal.*, 35:2440–2463, 1998.
- [14] D. Craiem, S. Graf, F. Pessana, J. Grignola, D. Bia, F. Gines, and R. Armentano. Cardiovascular engineering: modelization of ventricular arterial interaction in systemic and pulmonary circulation. *Latin American Applied Research*, 35:111–114, 2005.
- [15] J.E. Davies, Z.I. Whinnett, D.P. Francis, K. Willson, R.A. Foale, I.S. Malik, A.D. Hughes, K.H. Parker, and J. Mayet. Use of simultaneous pressure and velocity measurements to estimate arterial wave speed at a single site in humans. *Am. J. Physiol. Heart Circ. Physiol.*, 290:H878–H885, 2006.
- [16] K. Devault, P. Gremaud, V. Novak, M. Olufsen, G. Vernières, and P. Zhao. Blood flow in the circle of Willis: modeling and calibration. *Multiscale Model. Simul.*, 7:888–909, 2008.
- [17] L. Formaggia, J.F. Gerbeau, F. Nobile, and A. Quarteroni. On the coupling of 3D and 1D Navier-Stokes equations for flow problems in compliant vessels. *Comp. Meth. App. Mech. Eng.*, 191:561–582, 2001.
- [18] L. Formaggia, D. Lamponi, and A. Quarteroni. One-dimensional models for blood flow in arteries. *J. Eng. Math.*, 47:251–276, 2003.
- [19] O. Frank. Die Grundform des arteriellen Pulses. *Z. Biol.*, 37:483–526, 1899.
- [20] V.E. Franke, K.H. Parker, L.Y. Wee, N.M. Fisk, and S.J. Sherwin. Time domain computational modelling of 1D arterial networks in monochorionic placentas. *Mathem. Mod. and Num. Analysis*, 37:557–580, 2003.
- [21] Y.C. Fung. *Biomechanics: Mechanical properties of living tissues*. Springer-Verlag (New York), 2nd edition, 1993.
- [22] C.G. Giannopapa. *Fluid-structure interaction in flexible vessels*. Ph.D. thesis, University of London, 2004.

- [23] A.W. Khir, A. O'Brien, J.S.R Gibbs, and K.H. Parker. Determination of wave speed and wave separation in the arteries. *J. Biomech.*, 34:1145–1155, 2001.
- [24] P.A. Lynn and W. Fuerst. *Introductory digital signal processing with computer applications*. John Wiley & Sons, 1989.
- [25] K.S. Matthys, J. Alastruey, J. Peiró, A.W. Khir, P. Segers, P.R. Verdonck, K.H. Parker, and S.J. Sherwin. Pulse wave propagation in a model human arterial network: Assessment of 1-D numerical simulations against *in vitro* measurements. *J. Biomech.*, 40:3476–3486, 2007.
- [26] M.S. Olufsen, C.S. Peskin, W.Y. Kim, E.M. Pedersen, A. Nadim, and J. Larsen. Numerical simulation and experimental validation of blood flow in arteries with structured-tree outflow conditions. *Annals Biomed. Eng.*, 28:1281–1299, 2000.
- [27] G. Papadakis. Coupling 3D and 1D fluid–structure–interaction models for wave propagation in flexible vessels using a finite volume pressure-correction scheme. *Commun. Numer. Meth. Engng.*, 25:533–551, 2009.
- [28] T. Passerini. *Computational hemodynamics of the cerebral circulation: multiscale modeling from the circle of Willis to cerebral aneurysms*. Ph.D. thesis, Politecnico di Milano, 2009.
- [29] T. Passerini, M.R. De Luca, L. Formaggia, A. Quarteroni, and A. Veneziani. A 3D/1D geometrical multiscale model of cerebral vasculature. *J. Eng. Math.*, 64:319–330, 2009.
- [30] T.J. Pedley. *The fluid mechanics of large blood vessels*. Cambridge University Press, 1980.
- [31] J. Peiró and A. Veneziani. Reduced models of the cardiovascular system. In L. Formaggia, A. Quarteroni, and A. Veneziani, editors, *Cardiovascular Mathematics. Modeling and simulation of the circulatory system*, pages 347–394. Springer-Verlag (Milano), 2009.
- [32] A. Quarteroni, M. Tuveri, and A. Veneziani. Computational vascular fluid dynamics: problems, models and methods. *Comput. Visualization Sci.*, 2:163–197, 2000.
- [33] S.J. Sherwin, L. Formaggia, J. Peiró, and V. Franke. Computational modelling of 1D blood flow with variable mechanical properties and its application to the simulation of wave propagation in the human arterial system. *Int. J. Numer. Meth. Fluids*, 43:673–700, 2003.
- [34] S.J. Sherwin, V.E. Franke, J. Peiró, and K.H. Parker. One-dimensional modelling of a vascular network in space-time variables. *J. Eng. Maths.*, 47:217–250, 2003.

- [35] N.P. Smith, A.J. Pullan, and P.J. Hunter. An anatomically based model of transient coronary blood flow in the heart. *SIAM J. Appl. Math.*, 62:990–1018, 2001.
- [36] B.N. Steele, J. Wan, J.P. Ku, T.J.R. Hughes, and C.A. Taylor. *In vivo* validation of a one-dimensional finite-element method for predicting blood flow in cardiovascular bypass grafts. *IEEE Trans. Biomed. Eng.*, 50:649–656, 2003.
- [37] N. Stergiopoulos, D.F. Young, and T.R. Rogge. Computer simulation of arterial flow with applications to arterial and aortic stenoses. *J. Biomech.*, 25:1477–1488, 1992.
- [38] D. Valdez-Jasso, M.A. Haider, H.T. Banks, D.B. Santana, Y.Z. German, R.L. Armentano, and M.S. Olufsen. Analysis of viscoelastic wall properties in ovine arteries. *IEEE Trans. Biomed. Eng.*, 56:210–219, 2009.
- [39] S. Čanić and E.H. Kim. Mathematical analysis of the quasilinear effects in a hyperbolic model blood flow through compliant axi-symmetric vessels. *Math. Meth. Appl. Sci.*, 26:1161–1186, 2003.
- [40] S. Čanić, J. Tambača, G. Guidoboni, A. Mikelić, C. Hartley, and D. Rosenstrauch. Modeling viscoelastic behavior of arterial walls and their interaction with pulsatile blood flow. *SIAM J. Appl. Math.*, 67:164–193, 2006.
- [41] J.J. Wang, A.B. O’Brien, N.G. Shrive, K.H. Parker, and J.V. Tyberg. Time-domain representation of ventricular-arterial coupling as a windkessel and wave system. *Am. J. Heart Circ. Physiol.*, 284:H1358–H1368, 2003.
- [42] N. Westerhof, F. Bosman, C.J. de Vries, and A. Noordergraaf. Analog studies of the human systemic arterial tree. *J. Biomech.*, 2:121–143, 1969.
- [43] O.C. Zienkiewicz, R.L. Taylor, S.J. Sherwin, and J. Peiró. On discontinuous Galerkin methods. *Int. J. Numer. Meth. Fluids*, 58(2):1119–1148, 2003.

# MOX Technical Reports, last issues

Dipartimento di Matematica “F. Brioschi”,  
Politecnico di Milano, Via Bonardi 9 - 20133 Milano (Italy)

- 06/2010** JORDI ALASTRUEY, TIZIANO PASSERINI, LUCA FORMAGGIA,  
JOAQUIM PEIRÓ:  
*The effect of visco-elasticity and other physical properties on aortic and cerebral pulse waveforms: an analytical and numerical study*
- 05/2010** MATTEO LONGONI, A.C.I. MALOSSI, ALFIO QUARTERONI,  
ANDREA VILLA:  
*A complete model for non-Newtonian sedimentary basins in presence of faults and compaction phenomena*
- 04/2010** MARCO DISCACCIATI, PAOLA GERVASIO, ALFIO QUARTERONI:  
*Heterogeneous mathematical models in fluid dynamics and associated solution algorithms*
- 03/2010** P.E. FARRELL, STEFANO MICHELETTI, SIMONA PEROTTO:  
*A recovery-based error estimator for anisotropic mesh adaptation in CFD*
- 02/2010** PIETRO BARBIERI, NICCOLO' GRIECO, FRANCESCA IEVA,  
ANNA MARIA PAGANONI AND PIERCESARE SECCHI:  
*Exploitation, integration and statistical analysis of Public Health Database and STEMI archive in Lombardia Region*
- 01/2010** G.M. PORTA, S. PEROTTO, F. BALLIO:  
*Anisotropic Mesh Adaptation Driven by a Recovery-Based Error Estimator for Shallow Water Flow Modeling*
- 35/2009** C. D'ANGELO, P. ZUNINO:  
*Robust numerical approximation of coupled Stokes and Darcy flows applied to vascular hemodynamics and biochemical transport*
- 34/2009** P. F. ANTONIETTI, P. HOUSTON:  
*A Class of Domain Decomposition Preconditioners for hp-Discontinuous Galerkin Finite Element Methods*
- 33/2009** S. VANTINI:  
*On the Definition of Phase and Amplitude Variability in Functional Data Analysis*

**32/2009** S. MICHELETTI, S. PEROTTO:  
*Anisotropic adaptation via a Zienkiewicz-Zhu error estimator for 2D  
elliptic problems*